SPECIAL ISSUE ARTICLE

THE CANADIAN JOURNAL OF
CHEMICAL ENGINEERING

Image analysis for design and operation of gravity separators with coalescing aids

Jan Schäfer[1] | **Mark W. Hlawitschka**[2] | **Hans-Jörg Bart**[1]

[1]Fluidverfahrenstechnik, Technische Universität Kaiserslautern, Kaiserslautern, Germany

[2]Institut für Verfahrenstechnik, Johannes-Kepler Universität Linz, Linz, Austria

Correspondence
Hans-Jörg Bart, Fluidverfahrenstechnik, Technische Universität Kaiserslautern, Gottlieb-Daimler-Straße 44, Kaiserslautern, 67663, Germany.
Email: bart@mv.uni-kl.de

Abstract

In gravity separators, also known as settlers, two immiscible liquid phases separate due to differences in density. In extraction mixer-settler units, a dispersion needs to be separated within the separator unit. In order to overcome the hitherto purely experimental design, a knitted mesh adapted model as well as an automated test facility were developed in this work, which easily enable a scale-up to industrial units. An automation allows for a controlled investigation of knitted meshes as coalescing aids in settlers, and this was achieved via photo-optical probes with an optimized image analysis technique. It overcomes the limitations of neuronal network training based on manually annotating images using computer-generated image data. Therefore, the new methodology and setup are explained in detail, and the derivation and application of a new model to design separators with knitted meshes as coalescing aid is presented and compared to experimental results using meshes of different structures and materials. Finally, case studies and scale-up are discussed.

KEYWORDS
coalescing aids, convolutional neuronal network, horizontal gravity settler, image analysis

1 | INTRODUCTION

The phase separation of liquid–liquid mixtures in horizontal gravity settlers is found in many chemical engineering fields such as the chemical, pharmaceutical, biochemical, and petrochemical industries as well as hydrometallurgy. In the latter, gravity settlers are dominant when metal ions are recovered from low-grade ores after leaching and extraction with the help of liquid ion exchangers.[1] A typical apparatus has a diameter of 0.5–5 m and a length of 3–30 m, with costs involved (depending on pressure and material used) from 20 000 € to 1.000 000 €.[2] Despite the investment costs in the case of overdesign, a lot of liquid inventory is stored, which is

not useful for further processing. Coalescence aids will help in a size reduction of a gravity settler, but design and scale-up are very empirical.

In order to better understand the droplet settling process, driven by drag, buoyancy, and coalescence in a settler with coalescing aids, detailed investigations are necessary. It is markedly influenced by physical properties (viscosity, density difference, interfacial tension, and contact angle) and the resulting transient droplet size distribution (DSD), which influences the sedimentation speed of the droplets and thus their wetting and coalescence behaviour.[3–5]

There exist sampling methods and more or less invasive techniques in order to evaluate a DSD. In comparison

to other methods, as is the capillary suction probe,[6] needle probe,[7] wire mesh sensor,[8] laser-based,[9] and tomographic methods,[10] the image-based method is the most direct and accurate one, often used to calibrate other systems.[11,12] A newly developed optical multimode online probe (OMOP) device is used for optical analysis as described elsewhere.[13] The telecentric lens array, giving parallel light, allows distance-independent size detection via a shadowgraphic technique, and the transmitted light gives a high contrast. This is in contrast to an incident light method where the distance dependency is not negligible, as droplets farther away appear smaller. However, a problem arises at technically relevant high droplet phase fractions with plenty of overlapping, making an assignment of a certain droplet diameter difficult. Here, sophisticated image analysis tools come into play to retrieve detailed information at high accuracy and speed.

This paper presents a mixer-settler setup with a control loop for the mixer speed using the OMOP imaging probe and convolutional neural networks (CNN) for fast mean diameter evaluation. The training is carried out in a two-stage approach using generated images. In the first step, a CNN is trained to segment the distance transform of generated images of overlapping circles.[14] In the second step, this trained CNN is used to evaluate real experimental images to create a ground truth database for the final neural network segmenting live images. In that respect, an overview of the used image processing steps is given prior to their application in a settler. Finally, a design approach for horizontal settlers when using knitted meshes as coalescing aids is given.

2 | IMAGE SEGMENTATION VIA CNN

A standard CNN is inspired by the biological visual cortex and has many different ranges of applications, for example, image classification, speech, or handwriting recognition.[15] Such networks have two important processes, namely, feature extraction and down-sampling, which are used to extract and compress information from the images. Convolution and max pooling are the two operations used for this. After this down-sampling part of the CNN, a feed-forward neural network starts.[16] This allows the CNN to predict classes, vectors, etc., but not the segmentation of objects.

A CNN, which is capable of segmenting images locally, is U-net introduced by Ronneberger et al.[17] The network structure in this case is also a two-stage approach, but the second stage is different. Whereas a common CNN has a fully connected network in the second stage, a U-net-styled network has an up-sampling path. These layers consist of up-convolution and normal convolution operations in

which the network scales the feature maps, from the smallest size close to the original size of the input image. With this, it is possible to segment objects in the image locally. The trained U-net learned in the down-sampling path to extract the important features for the segmentation and in the up-sampling path to get these features to a segmentation mask. For each pixel in the image, U-net predicts the probability that the pixel belongs to the previously specified classes. In an image of droplets, the background can be one class and the droplets another. These classes are set in the ground truth images used for training.

U-net then predicts the probability if a pixel belongs to the background or a droplet. An example of a U-net style CNN with four layers and four filters is shown in Figure 1. The filters in this case are the kernels, and their number is adapted in the layers of the network by the following process. In each of the i layers there are $2^{(i+4)}$ kernels that will be learned, which is true for the down- and up-sampling paths. The numbering of the layers starts with 0, this means that in the fourth layer of the network, there are $2^{(3+4)} = 128$ feature maps.

To train a U-net style CNN, a database is needed that consists of the images that should be segmented and their already known segmentation. This requires usually manual evaluation of the images in question and is time and labor intensive. This can be overcome by using generated images. The main idea for creating generated images with a good representation of the real experiment is similar to the feature extraction of CNNs. Both, the generated images and the ones acquired in the experiment are pre-processed in a way that only the feature of interest for the segmentation task is used as an input for the CNN. Since the droplets are spherical, the most important information about them can be represented using the Euclidean distance transform of the images. This calculates the minimal distance of each pixel to the next boundary pixel, in a binary image. An example of this distance transform can be seen in Figure 2 in the left image.

Figure 1 depicts that an overall network was used for the segmentation of distance transforming images, using artificially created images as a training database. Table 1 lists all the hyperparameters used in the training. The detailed training process is described in Schäfer et al.[14]

2.1 | Post processing the output of the CNN

The final output of the CNN is a segmentation mask (see Figure 2 right image), which has to be post processed for evaluating the DSD. The segmentation between the different particles is visible as darker lines in the image, and the particles are marked as brighter areas. Still challenging are areas with many overlaying particles, where no

FIGURE 1 U-net graph representation used for the segmentation of distance transform. ReLU, rectified linear unit
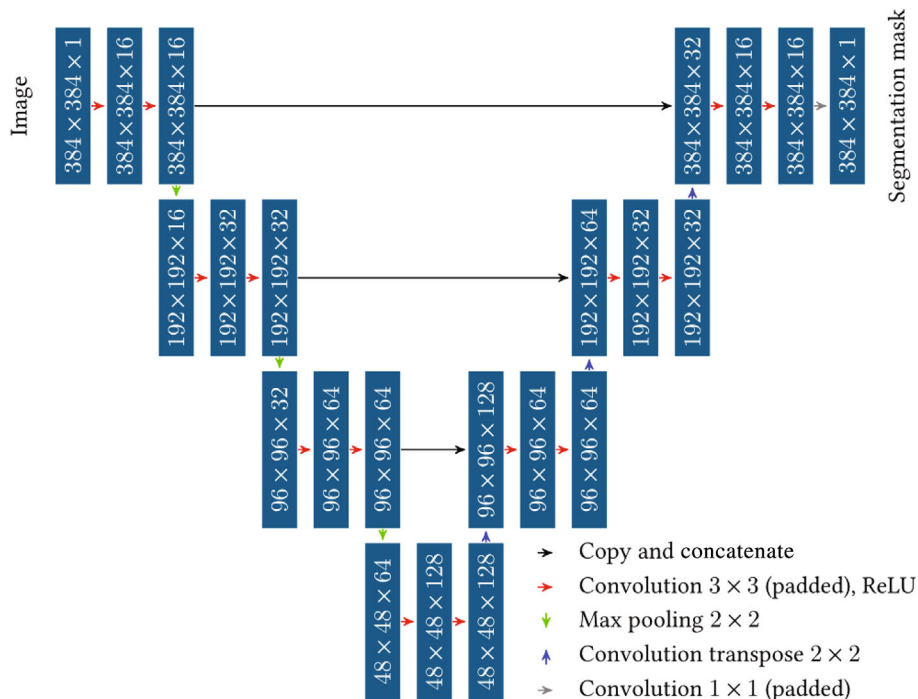

FIGURE 2 Sample images used for training the convolutional neural networks (CNN) and prediction of the network (input, ground truth, and predicted segmentation map). CNN, convolutional neural networks
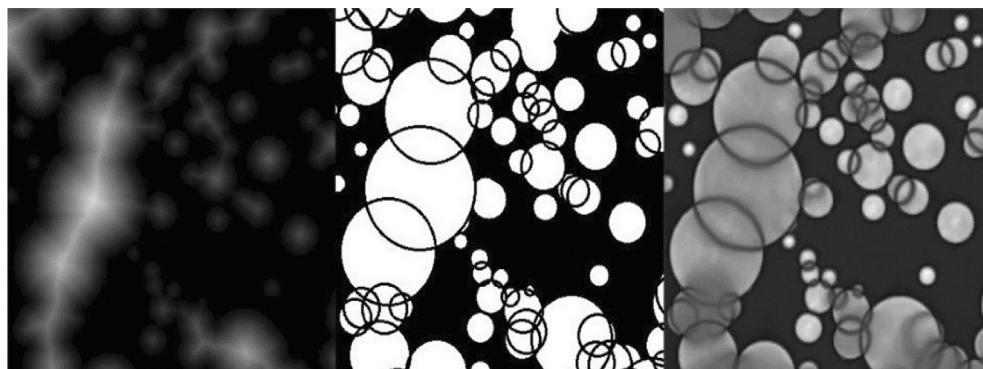

TABLE 1 Hyperparameters for training the U-net style convolutional neural networks (CNN)

Parameter	Value
Learning rate (Lr)	10^{-4}
Momentum (m_{m})	0.99
Weight decay (w)	$5 \cdot 10^{-4}$

Abbreviation: CNN, convolutional neural networks.

TABLE 2 Settings used to control the image acquisition, in the Basler camera in python

Setting	Value
Resolution	1024×1024 pixel^2
Exposure time	$20\ \mu s$
Frame rate	50 FPS

clear segmentation can be found. The approach uses an Otsu threshold operation to segment the particles into single contours.[14]

Overlapping droplets are segmented in this case into more than two contours in many cases. To find the corresponding parts forming one droplet a circle is fitted to all the neighbouring contours and compared to the area of the single surfaces. If the fitted circle and the sum of the areas match, this is considered to be on droplet. A flow chart of this evaluation process is shown in Figure 3. This

describes the first step of the training process used in this paper, and in the next section, this is adapted for the evaluation of live camera images.

2.2 | Adaption of the training for the direct segmentation

The approach using the distance transform for the segmentation requires a preprocessing of the images acquired by
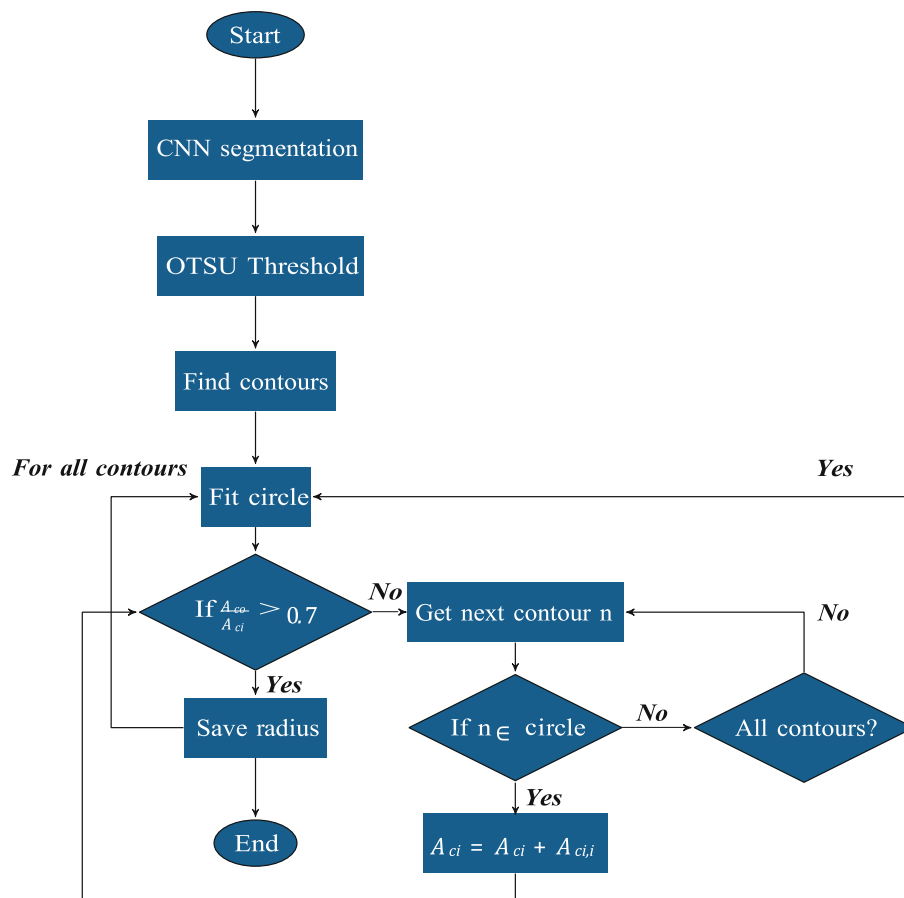
FIGURE 3 Flow chart of the post-processing algorithm used to assign a diameter to the particles segmented by the trained U-net. ci, circle; CNN, convolutional neural networks; i, index

the OMOP system, which could potentially falsify the results of the CNN evaluation in varying lighting conditions or recording quality. As a solution to this, the second step was to use the trained CNN to create an annotated database with the real OMOP images as input and the threshold of the segmentation mask, the predicted segmentation of the trained U-net as ground truth. With this database, a second U-net was trained, which is able to directly evaluate the OMOP images. It is important to note that this is not entirely possible without any pre-processing. The network needs to be trained on consistent data in order to improve the training process. Since it cannot be assured that all the images acquired in the experiment have the same exposure, and, due to the shadow graphic imaging, the lighting conditions change with the phase fraction of the particles, and this needs to be addressed. As an example, during training, the background would have different pixel intensities and the network is hindered from finding consistent parameters to extract these. A solution to this problem is to use the histogram equalization over the whole OMOP image database. Compared to the pre-processing using the distance transform, which extracts information from the image and might only change pixel intensities, it is less intrusive. Without the pre-processing using the distance transform, the network needs to find a way to extract the important features for the segmentation from the original image, which increases the complexity of the task. To cope with this, the number of layers and kernels, the U-net style CNN available for this procedure was changed. Here, the values of the paper of Ronneberger et al. were used with five layers and six kernels. The patch size was increased to 512×512 pixel^2 images as the input for the CNN. The other hyperparameters used for training were the same as before (see Table 1). The training was performed on a Nvidia Tesla V100, which allowed for a faster completion and a batch size of six images. Figure 4 shows the evaluation of the trained U-net.

The predicted segmentation mask shows a clear distinction between the background, the particles, and the boundaries of the particles. As a post-processing algorithm (to fit a droplet size to the different contours in the segmentation mask), the same process is used as depicted in Figure 3. This results in a simplified image evaluation process with less computational costs.

Figure 5 shows the activation of some learned kernels in the network. The first convolution layer shows again rough image translations with varying intensities of the
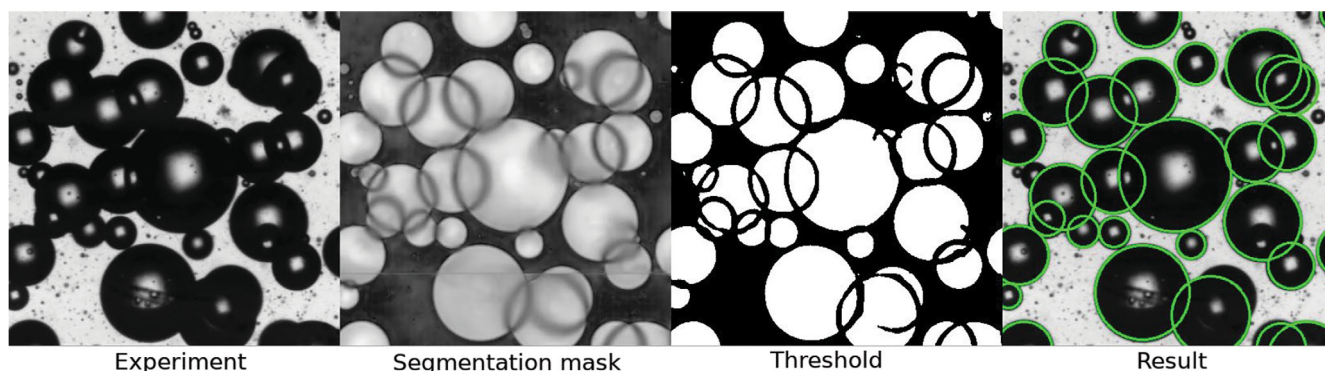
| Experiment | Segmentation mask | Threshold | Result |

FIGURE 4 Example images of the evaluation using the trained U-net to segment optical multimode online probe (OMOP) images. OMOP, optical multimode online probe
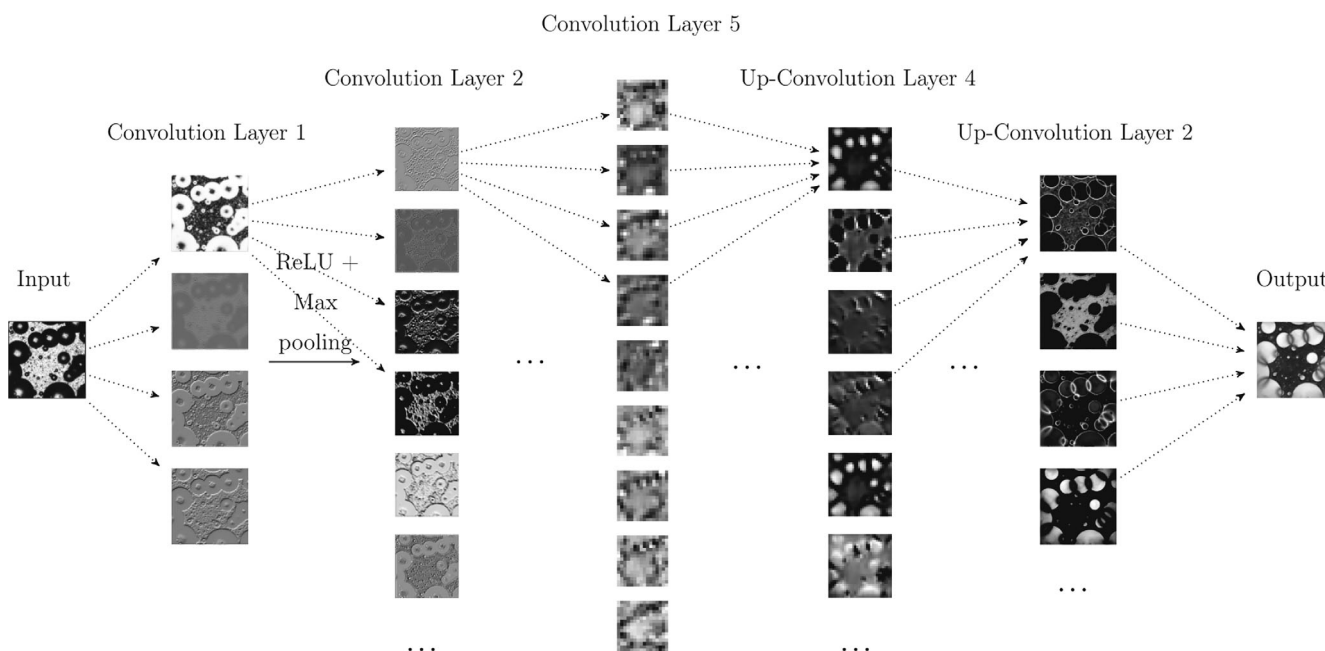

FIGURE 5 Graphical representation of the activation on a subset of kernels in different layers of the U-net trained to segment optical multimode online probe (OMOP) images. OMOP, optical multimode online probe; ReLU, rectified linear unit

particles and the background. The first few kernels show different intensities between particles and background, directional highlighted edges (image 3 and 4 of layer 2) and different sizes of the particle surfaces. In the up-sampling path of the U-net trained to segment OMOP images, already in the lowest up-sampling layer, clear structures of the particle segments are visible. In the up-sampling path, the network learned to combine the different extracted features, which propagate through the down sampling path with different intensities and grow them to areas that represent the final segmentation of the network. This results in the segmentation mask, where each pixel has been assigned a probability of belonging to the predefined classes. In this case, the two classes are background/particle borders and particles (the borders between the particles and the background belong to the same class).

2.3 | Implementation of a trained CNN in a control loop

The U-net trained to segment images acquired by the OMOP can be used to create a process control loop able to regulate the rotation speed of a mixer dependent on a set mean droplet target diameter. This control loop is integrated into the mixer-settler setup (see Figure 6) and is used to guarantee a specific constant mean
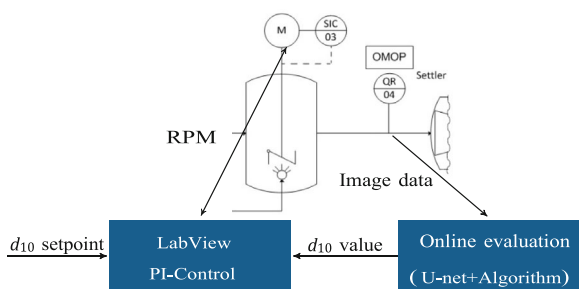
FIGURE 6 Control loop used to set the mean diameter in the mixer-settler setup. The evaluation program is written in Python (version 3.2) and manages the image acquisition via a Basler camera, using the settings shown in Table 2. After acquisition the image is split into patches of the size 512×512 pixel^2, used to train U-net, and evaluated by the trained network. The camera resolution of 1024×1024 pixel^2 was chosen so that there is no excess, while splitting the image. After the segmentation through the trained U-net, the resulting segmentation mask is rearranged to the original resolution. This image is then evaluated using the algorithm shown in Figure 3. OMOP, optical multimode online probe; PI, proportional integral controller; QR, quality recording; RPM, rotation per minute; SIC, frequence indication control

diameter during the experiments. The control setup consists of the OMOP, acquiring live images of the droplets at the inlet of the settler, and U-net in combination with an evaluation algorithm calculating the mean diameter. This is used in combination with a LabView proportional integral controller (PI) to adjust the mixer speed on the basis of the evaluated images to control a given mean droplet diameter (d_{10}).

The main problem with the image capturing is that the captured DSD in one image cannot be considered representative for the whole process. To have a statistically significant representation of the DSD, the moving average of the last 2000 measured droplets is calculated, which results in a new mean diameter for each image. An example of the working control loop is shown in Figure 7. Here, a continuous water phase is mixed with paraffin oil at a constant phase ratio of 15% and a constant total flow rate of 0.2 m^3/h, while the mean diameter is changed. The diameter variation is done every 5 min with the following steps: d_{10} = 0.35, 0.4, 0.35, 0.375 mm.[18]

The diagram shows that the mean diameter is fluctuating around the target value. The set time for a new target diameter is dependent on the difference between the two set diameters. In the case of this example, setting d_{10} = 350 to d_{10} = 400 μm takes about 120 s to set the new target diameter. This is also dependent on the direction of the change, if the diameter is in- or decreased, due to the inertia of the mixed fluid system.

3 | DROPLET BEHAVIOUR IN A GRAVITY SETTLER

Settlers are classified by their height to length ratio into vertical and horizontal settlers. A vertical settler, with a height to length ($\frac{H}{L} < 2$), is usually operated in counter current flow, for example, at the head of an extraction column. The separation in horizontal settlers ($\frac{H}{L} > 2$), as shown in Figure 8, is performed in co-current flow.[19] The dispersion enters the settler at the inlet in the middle of the apparatus. In the transition zone, the cross-section of the settler increases to its maximum diameter, and for a DN100 settler, this is 100 mm. This reduces the flow speed of the dispersion and eases the flow conditions. After a turbulent region at the inlet, further into the settler, there should not be any turbulence disturbing the separation of the two phases.

Depending on which phase is dispersed, the lighter dispersed phase rises or the heavier dispersed phase descends to the surface in the settler due to density differences. The droplets form a film at the surface, which is called the densely packed dispersion layer. In this laminar flowing layer, the droplet size increases due to droplet–droplet coalescence until the droplet coalesces with the now continuous phase at the surface. The settling process is governed by two main factors, sedimentation of the dispersed phase at the surface and coalescence of the droplets, either with each other or with the continuous surface of the main liquid and are influenced by different properties of the fluids involved.[19] The first process is dependent on the buoyancy, inertia, and drag force. These are again influenced by, for example, the density difference between the fluids, the viscosity of the continuous phase, the initial DSD of the dispersed phase, the flow speed, the interfacial tension, and the phase ratio between the two fluids and determine the sedimentation of the droplets to the surface. The huge number of influences led to a variety of correlations, each valid for specific conditions.[20–22] The second process, the coalescence, is affected by the interfacial tension, the continuous phase viscosity, the phase fraction, density, surfactants, and the DSD, as it is given in correlations describing coalescence of droplets.[23,24]

Dependent on which of the two processes is the dominant factor, the settling process can be distinguished into a sedimentation- or coalescence-driven operation. A sedimentation-driven process can be improved through a larger (shallower) settler, where the droplets travel only a small way to the surface between the two phases. Other improvements are the usage of horizontal plates, which reduce the total height a droplet required to travel to reach the surface by creating multiple surfaces. This also

FIGURE 7 Variation of the target mean diameter and the mixer rotation per minute (RPM) adjustment of the control loop. RPM, rotations per minute
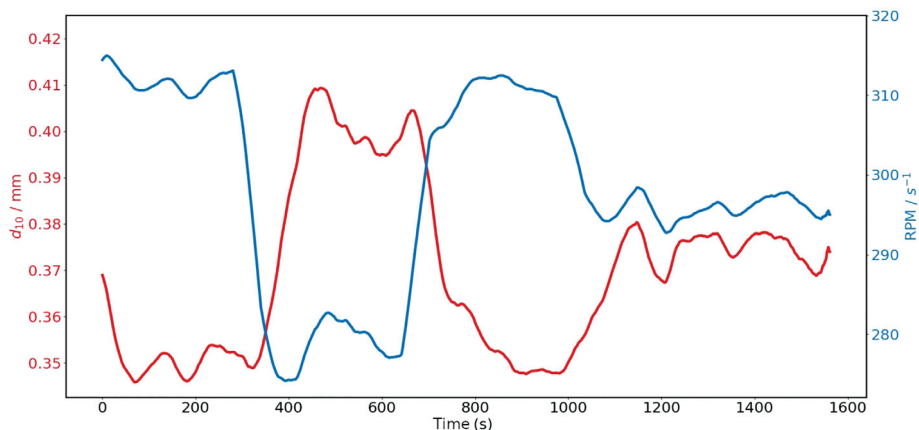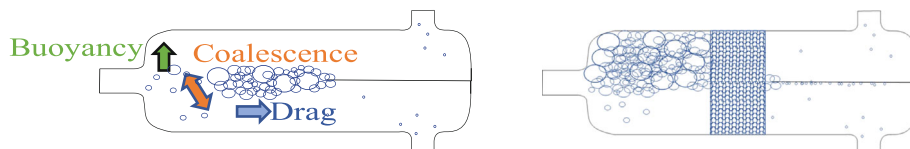

FIGURE 8 Illustration of a dispersion in a gravity settler without (left) and with knitted mesh (right)

increases the coalescence probability.[25] A coalescence-driven settling process can be improved by increasing the time droplets are in contact with each other or the surface between the two phases. This can be achieved by using internals, a simple example is vertical plate, close to the inlet of the settler. The droplets collide with the plate, which raises the contact probability between droplets and calms the flow conditions behind the plate. Other coalescing aids in this context are the aforementioned horizontal plates, fibre beds, and knitted meshes.[19] The latter are part of this investigation. Figure 8 shows a dispersion wedge in a settler without internals and the accumulation of the dispersion in a settler with a knitted mesh as a coalescing aid.

In a settler without internals, the dispersion wedge can form freely, the droplets are densely packed at the surface. If the wedge reaches the end of the settler, a dispersion band forms.[19] With a knitted mesh as an internal in the settler, this wedge is accumulated in front of the mesh. The goal of the usage of a mesh is to reduce the wedge length and to increase the maximum throughput or the needed length of the settler by promoting the coalescence of the dispersion. The main assumption is that droplets larger than the pores of the mesh are retained and the smaller droplets have a chance to wet the surface of the mesh fibres, which increases the coalescence probability by increasing the contact time with other droplets when being trapped on the fibre.

Knitted meshes consist of a variety of materials and different structures. The composition of such a mesh consists of a fibre, which is woven into a layer and these layers can be arrange in different ways to form the final

mesh. One option is to roll them along their length. This results in a layer alignment in flow direction in the settler, this is called a wrapped mesh. The second option is referred to as 'layered' and aligns the mesh in a sinuous line and wraps them in a last layer mesh. In the settler, the layers are perpendicular to the flow direction. The different alignments are shown in Figure 9.

The layers of these knitted meshes can be produced using different materials, ranging from glass over polymers to metal fibres. A special case is composite meshes, where in the layer of the knitted mesh other materials are woven between the fibres. Part of this investigations are five different meshes, with different materials and different structures. The meshes can be categorized using the package density and the effective surface. The package density of a knitted mesh is calculated using the total volume of the bounding box in reference total weight of the mesh. The denser a knitted mesh is packed, the closer the package density is to the material density.

$$\rho_{pa} = \frac{m_{mesh}}{V_{mesh}} \qquad (1)$$

The meshes investigated as coalescing aids are used for the separation of large droplets, which means the package density is significantly smaller than the material density, and with that, the porosity of the knitted mesh is higher. Table 3 shows the properties of all the investigated knitted meshes. To distinguish between the different mesh configurations, each mesh gets assigned a label. Here, perfluoroalkoxy alkane (PFA) 0.27 represents the PFA mesh with a 0.27 mm wire thickness, both variants

with the same mesh length (100 mm). The label for the stainless-steel mesh VA50 distinguishes them by their mesh length, of 50 or 100 mm, and both have the same wire thickness (stainless steel, notation derived from steel grades V1A, V2A, etc.).

3.1 | Experimental results of laboratory-scale investigations in a DN100 settler

In the laboratory-scale settler experiments, the efficiency of the different meshes to reduce the densely packed dispersion layer is investigated. The experiments are carried out in two steps. First, a set of reference experiments in a settler without internals was done. The target value of these investigations was the volume of the dispersion layer and the length and height of the densely packed dispersion wedge. In the second step, the same experiments are repeated with the knitted meshes as different internals, comparing the height of the layer in front of the mesh to the height of the surface behind the mesh. The above presented control loop (see Figure 6) is used in combination with an automated flow rate control for oil and water to generate a defined mean droplet diameter using the online CNN evaluation of the OMOP images. This setup enables experiments where only one parameter in the settler system is changed, as depicted in Table 4.

The dispersion wedge length without internals and the reduction of the dispersion wedge with the knitted meshes are evaluated using a DSLR camera (Nikon D5600) in front of the settler. This camera captures the whole settler length in a single image. An automatic acquisition is triggered every minute during the experiment. The data collected from the measuring equipment connected to the settler and the images acquired by the camera are sorted using the corresponding time stamps. The glass settler is illuminated using a light-emitting diode (LED) panel behind the settler. The densely packed layer refracts the transmitted light in such a way that there is a sharp contrast between the layer and the surrounding fluid. This allows a segmentation of the dense dispersion layer in the images to measure the height and length of the dispersion wedge in the experiments without internals. The algorithm used for evaluation with knitted meshes is described in the following passage. The
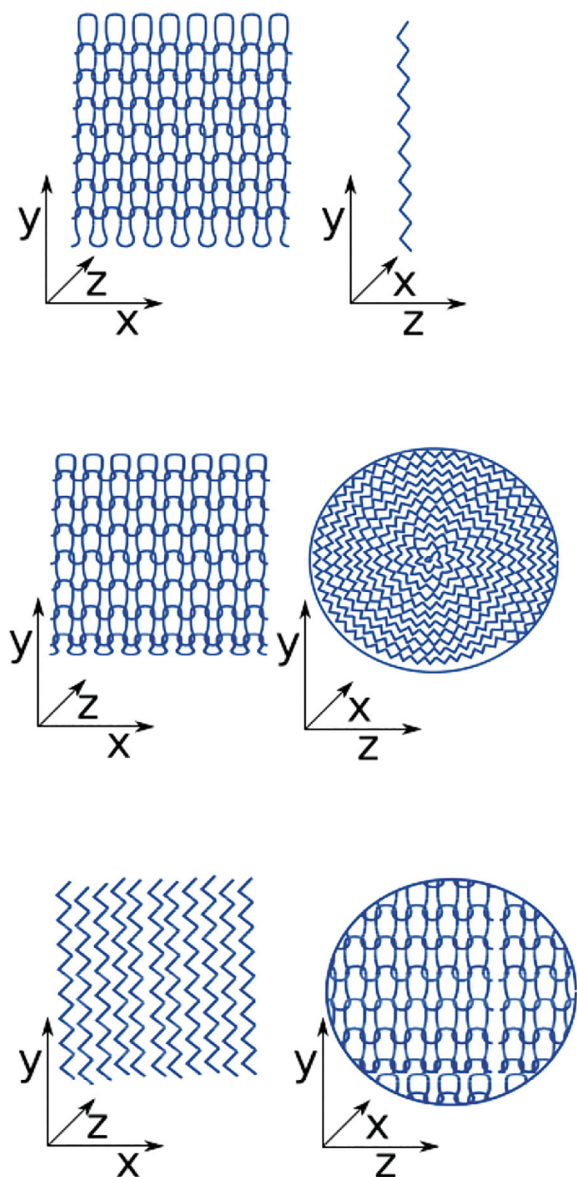

FIGURE 9 Different knitted mesh layer alignments (top one layer, middle wrapped, and bottom layered)

TABLE 3 Properties of the investigated knitted meshes

Label	Material	Structure	Packing density (kg/m)^3	Fibre width (mm)	Length (mm)
Combination	VA + glass	Wrap	300	0.27 (0.28)	100
PFA 0.27	PFA	Layered	145	0.27	100
VA100	VA	Wrap	300	0.27	100
VA50	VA	Wrap	300	0.27	50

Abbreviations: PFA, perfluoroalkoxy alkane; VA, stainless steel.

main goal of the evaluation with a knitted mesh as a coalescing aid was to measure the accumulation height of the dispersion in front of the mesh, as well as the length reduction of the dispersion wedge compared to the empty settler. The height of the densely packed layer in front of the mesh, the level of the surface behind the mesh, or if the dispersion wedge permeated the mesh, and the height of the dispersion behind the mesh are part of the measurements. The images are sorted similar to the experiments without a mesh. After that, two slices from every recorded image are extracted. One right in front of the

TABLE 4 Experimental series of the settler investigations

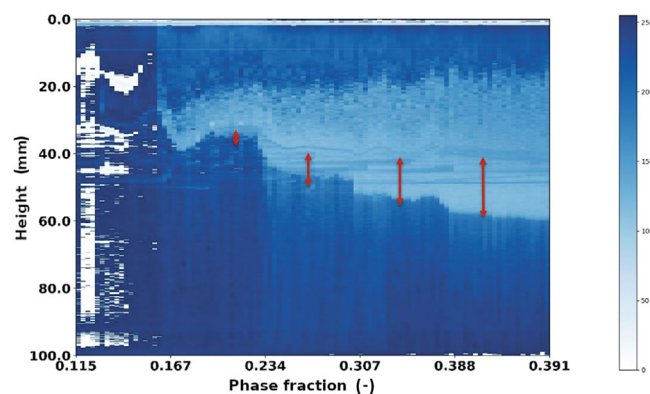| Label	Variation	Fixed
E1	Total flow rate	d_{10}, phase fraction
E2	Phase fraction	d_{10}, total flow rate
E3	d_{10}	Total flow rate, phase fraction

FIGURE 10 Evaluated image of the algorithm to determine the height difference of the dispersion wedge (arrows marking height difference in front and behind mesh)

mesh, and the other behind the mesh. The size of these slices is the whole height of the settler and 10 pixels in length for both positions. To cope with droplets wetting the glass surface of the settler and blocking the visibility of the dispersion wedge in certain areas, the slices are calculated as the average of the seven neighbouring slices in the image. The resulting two slices are then used to calculate the difference between the two. This difference in images then allows the height difference between the dispersion wedge in front of the mesh and the surface behind the mesh to be determined. These images are then concatenated in such a way that, over the length of the newly created image, the time variation of the experiment is depicted. Figure 10 illustrates a resulting image of this operation. The y-axis shows the height of the settler in the image, whereas the x-axis depicts the change of the phase ration over time during the experiment. Each slice in the image (10 pixel) marks a point in time in the experiment where the dispersion in front of the mesh is compared to the dispersion behind the mesh, using the difference in greyscale values. This is depicted by the colour scale on the right side of the image. The lower level of the dispersion in front of the mesh is starting from a phase fraction of 0.167, clearly visible. This marks the point where the dispersion reaches the knitted mesh. Starting with a phase fraction of 0.234, there is a clear difference visible between the level of the dispersion in front of and behind the mesh marked by the red arrow.

The images are then evaluated manually using the measurement tool for length in ImageJ. The arrows in the image show the height of the dispersion layer in front of the mesh, at the bottom and the height of the surface behind the mesh at the top. Over time and with increasing phase fraction, under constant droplet diameter and

FIGURE 11 Comparison between the height difference of the dispersion in front and behind the different knitted meshes. COMB, combination; PFA, perfluoroalkoxy alkane
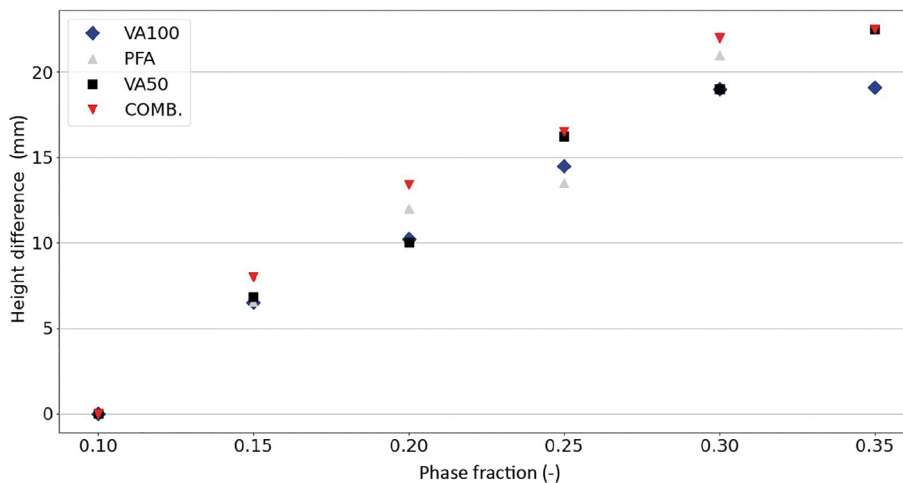
flow rate, the height difference between dispersion in front and behind the mesh increases.

Figure 11 shows the comparison of the height difference for the investigated meshes in the experimental series E2. Here, the mean diameter at the inlet ($d_{10} = 350\,\mu m$) and the total flow rate ($\dot{V} = 0.2\,\frac{m^3}{h}$) are constant, and the phase fraction increases periodically. The graph shows that with an increasing phase fraction of the oil, the accumulation height in front of the mesh increases. The slope of the curve decreases with higher phase fractions. This could be due to not only the properties of the meshes but also the chosen surface level in the settler, which was above the centre line. The further the level of the dispersion comes to this centre line, the greater the volume the dispersion can occupy in the cylindrical settler. Between the different materials, there was no great height deviation. At a phase fraction of 20%, the stainless-steel knitted mesh with a length of 50 mm (VA50) was percolated by the dispersion. Compared to the longer version of the same mesh, the accumulation of the dispersion in front of the mesh was the same. This results in a shorter length over which this height difference of dispersion in front of the mesh and the surface behind the mesh can be reduced, leading to a higher dispersion flow speed inside the mesh. An example of this is shown in Figure 12.

For the mesh with double the length, the breakthrough point was at twice the accumulation height of the shorter mesh. This shows that the dispersion speed inside the mesh plays a major role in dispersion breakthrough under otherwise constant conditions. The resulting angle between the mesh front and the surface behind the mesh was determined to be 72° at the breakthrough point. The optimal operating point of the knitted mesh should be where the lower end of the densely packed layer in front of the mesh is in the centre line of the settler. Here, the height difference between the accumulation in front and the surface behind the mesh is minimal, and with that, the flow speed of the dispersion in the mesh is minimal, assuming a cylindrical settler. The dispersion, which percolated the knitted mesh and forms a wedge behind the mesh, consists mainly of small droplets. This means the mesh classifies the dispersion; the larger droplets coalesce with the oil or wet the mesh. The smallest droplets, which represent the lowest layer in the dispersion wedge, are too small to wet the large wires and flow through the mesh if their speed is too high. This depends on surface nature, mesh length, and porosity as mentioned before.[18]

However, one can find different characteristics in the way the dispersion accumulates in front of the mesh. Depending on which phase better wets the material, the knitted mesh either supports the water or the oil phase. An example of this can be seen in Figure 13, where the black line marks the surface between the continuous oil and the dispersion. The PFA prefers wetting the oil phase. This leads to a capillary effect supporting the surface of the oil, and the dispersion accumulates in front of this oil surface. The wetting leads to a force directed downwards, pushing onto the dispersion and accumulating it in front of the oil phase. The stainless-steel prefers to wet with the water, and with that, the surface of the water is stabilized. This leads to a force directing the
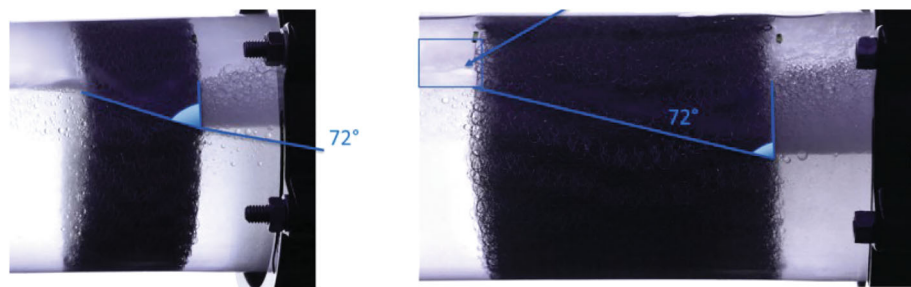

FIGURE 12 Breakthrough point at which the dispersion percolates the knitted mesh (left: length 50 mm, 20% phase fraction; right: length 100 mm, 40% phase fraction)
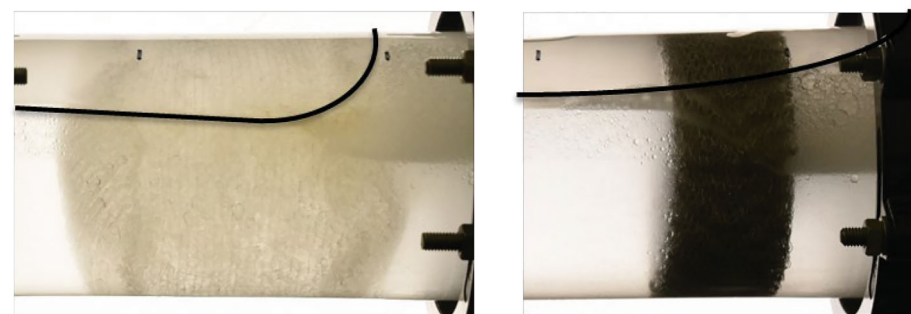

FIGURE 13 Accumulation of the dispersion wedge in front of perfluoroalkoxy alkane (PFA) (left) and stainless-steel mesh (right). PFA, perfluoroalkoxy alkane

dispersion upwards and accumulating the dispersion wedge in front of the water phase.

The breakthrough point in the experiment E3, where the inlet diameter d_{10} was varied, showed that this point is dependent on the diameter of the droplets. The smaller the droplets, the earlier the dispersion percolates the knitted mesh. An example of this is shown in Figure 14. The surface between water and oil in the images is at a height of 30 mm. The breakthrough point is marked by the red dot in the image. For the short mesh with a length of 50 mm, the dispersion starts to percolate the mesh at a mean diameter of $d_{10} = 0.375$ mm. The longer mesh can retain the dispersion until a mean diameter of $d_{10} = 0.325$ mm is reached. This can be explained by the aforementioned speed of the dispersion in the mesh. The smaller the droplets, the longer they have to be inside the mesh to be separated. Another explanation for this is that with smaller droplets, the height difference between the
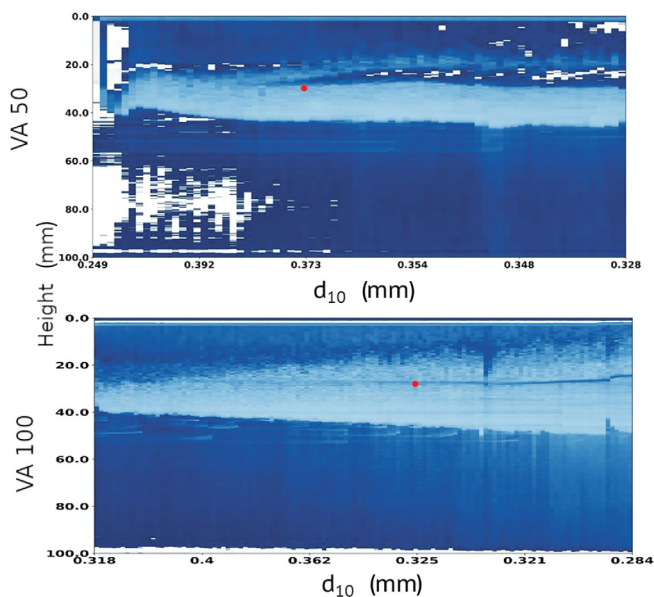
dispersion in front and the surface behind the mesh increases, which increases the flow speed of the dispersion in the mesh. The accumulation height at the breakthrough point for the shorter mesh was 13.94 mm, and for the longer mesh, it was 18.94 mm. This leads to the insight that the smaller the mean diameter of the particles at the inlet, the longer the mesh should be.

4 | MODELLING OF A SETTLER WITH KNITTED MESHES

In this section, a standard modelling approach of a phase separation in an empty horizontal gravity settler after Henschke[19] is further developed for knitted meshes as coalescing aids. The settler (see Figure 15) is divided into dl length and dh height elements. The iterative process calculates for each length and height element the change in droplet size due to droplet–droplet coalescence for the layers below the surface. At the surface, the loss of dispersion is calculated due to droplet–surface coalescence, and the new dispersion height in the next length element is determined. This process is repeated for each length element, either until there is no dispersion volume left or the end of the settler is reached.

The model provides the length of the dispersion wedge and allows for an approximation of the needed settler length. The calculations in each iteration are as follows. In a first step, the sedimentation length L_{in} is calculated. This describes the region at the inlet of the settler, where the droplets of the dispersion settle to the surface, and after the region, a dispersion wedge is formed.

$$L_{in} = 43.7 \left(\frac{d_{32,0}}{d_{32,0}+H_{p,0}} \right)^{0.4} \left(\frac{Re_{in}Re_s}{Ar} \right)^{0.5} \left(\frac{\Delta\rho}{\overline{\rho}} \right)^{0.2} \left(\frac{d_{32,0}}{D_s} \right)^{0.1}$$

(2)

FIGURE 14 Comparison of the experiment varying the inlet mean droplet diameter between a mesh with 50 and 100 mm length at 20% phase fraction and 0.2 m³/h total flow rate
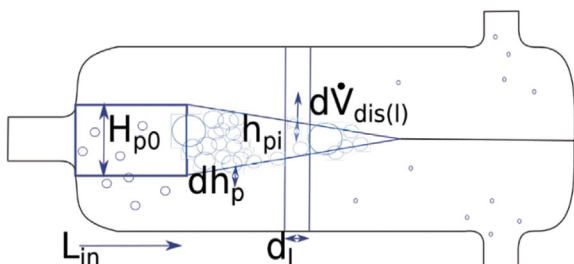

FIGURE 15 Modelling the separation in a gravity settler. dis, dispersion; i, index; l, length, p, packed dispersion
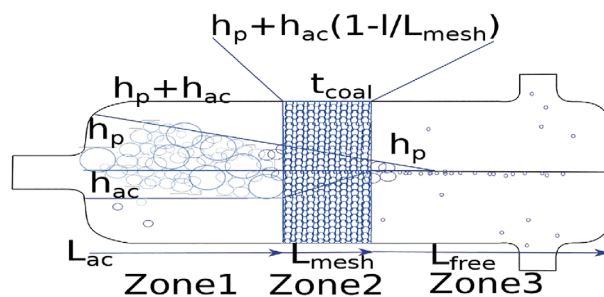

FIGURE 16 Modelling the separation of a dispersion with a knitted mesh as a coalescence aid. ac, accumulation of the dispersion; coal, coalescence; p, packed dispersion

TABLE 5 Comparison of the adapted modelling and experimental results for a DN100 settler

| Phase fraction | Wedge length | | | |
	Experiment empty (cm)	Henschke model (cm)	VA50 after mesh (cm)	Henschke model after mesh (cm)
20%	25.3	24	0	0
25%	30	28	0.5	0
30%	33.8	34	3.1	3
35%	42	38	7.2	8

In the case of the executed experiments, there was no clear sedimentation zone seen as described by Henschke,[19] and for this reason, the calculation of the inlet zone was disregarded. A reason for this could be the minimally invasive OMOP probe at the inlet of the settler. After this inlet zone, the dispersion wedge starts with the initial height $H_{p,0}$. The dispersion flow rate is determined by:

$$\dot{V}_{dis} = \frac{\dot{V}\alpha_0}{\alpha_p}. \tag{3}$$

The holdup inside the densely packed dispersion α_p is assumed in this case to be $\alpha_p = 0.9$, and α_0 is the phase fraction at the inlet. The retention time of the droplets in a length element of the settler is needed to calculate the change in the droplet size and is acquired by the following equation:

$$dt = \frac{h_p D_s dl}{\dot{V}_{dis}} \tag{4}$$

The starting point for the droplet size change calculation is the initial Sauter mean diameter at the inlet. In each height element, the coalescence time τ_{di} of the droplets is modelled using the following set of equations:

$$\tau_{di} = 7.65\mu \frac{R_a^{\frac{7}{3}}}{H_{cd}^{\frac{1}{6}}\sigma^{\frac{5}{5}}R_f r_s^*}$$

$$R_a = 0.5 d_{32}\left(1 - \left(1 - \frac{4.7}{4.7 + \mathrm{La_{mod}}}\right)\right)^{0.5}$$

$$R_f = d_{32}\left(1 - \frac{4.7}{4.7 + \mathrm{La_{mod}}}\right)^{0.5}$$

$$\mathrm{La_{mod}} = \left(\frac{\vec{g}\Delta\rho}{\sigma}\right)$$

$$H_{cd} = 10^{-20} \tag{5}$$

The parameter r_s^* can be estimated from the resulting coalescence curve of the sedimentation cell experiments presented in the work of Henschke,[19] using iterative modelling for stationary settling processes. The modelling approach is extended to include knitted meshes in the iterative calculation. This necessitates creating different zones (see Figure 16) in the modelled settler, where the calculation of the coalescence time, τ_{di}, is adapted.

The first zone (zone 1) starts with the inlet of the settler and ends at the starting position of the knitted mesh (L_{ac}). The second zone (zone 2) starts and ends with the mesh (L_{mesh}) and the third zone (zone 3) accounts for the rest of the modelled settler (L_{free}). The changes in the modelling approach in the different zones are based on the observations made in the settler experiments. The different experiments showed that the dispersion wedge accumulates in front of the knitted mesh, resulting in a greater dispersion height. This height is measured in the laboratory-scale experiments and used in the modelling to scale-up settlers with knitted mesh as internals. This means in zone 1 of the model, the measured height difference between the dispersion in front and after the mesh is added to the calculated dispersion height of the standard model.

$$h_{p,i} = h_{p,i} + h_{ac} \, for \, l \in [0, L_{ac}] \tag{6}$$

This results in a changed coalescence time because of the higher hydrostatic pressure and, with that, a greater loss of dispersion due to coalescence in front of the mesh, as seen in the experiments. In zone 2, it is assumed that, similar to the observations in Figure 12, the dispersion is reduced linearly over the mesh.

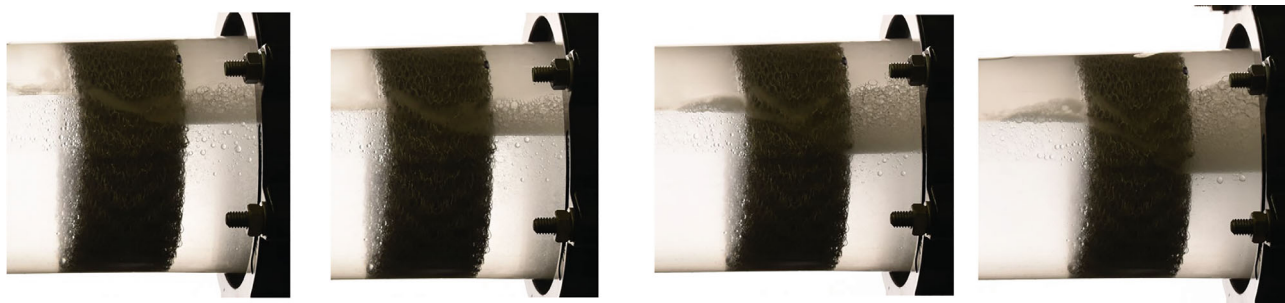$$h_{p,i} = h_{p,i} + h_{ac}\left(1 - \frac{l}{L_{mesh}}\right) \, for \, l \in \,]L_{ac}, L_{ac} + L_{mesh}] \tag{7}$$

FIGURE 17 Dispersion wedge (inflow from the right in a VA50 mesh) at different phase fractions (20%, 25%, 30%, 35% at 0.2 m³/h)

TABLE 6 Scale-up modelling with constant accumulation of the dispersion in front of the mesh

Phase fraction	Henschke model (cm)	Wedge length	
		Henschke modified VA50 (after mesh) (cm)	Henschke modified VA200 (after mesh) (cm)
20%	47	41 (18)	32 (0)
30%	66	61 (38)	50 (12)

TABLE 7 Scaling factor calculation assuming a linearly accumulating wedge

Phase fraction	Experiment (DN100) (mm)	Accumulation height (mm)	Factor
20%	253	10	$\frac{10}{253} = 0.0039$
30%	338	20	$\frac{20}{338} = 0.0059$

The effect of the mesh fibres on the coalescence in the dispersion wedge is modelled by introducing a modifier (t_{coal}) for the calculated coalescence time (τ_{di}) of the standard model in this zone. This modifier can be gathered using the laboratory-scale settler experiments, which are needed for the accumulation height of the dispersion anyway. The modification factor can be fitted by using the modelling approach for the laboratory-scale settler and the known dispersion wedge lengths measured in the experiments with the knitted mesh. The factor is adapted until the experimental and the modelling results match.

In the last zone, zone 3, the model is not changed, and it is assumed that the coalescence after the mesh is comparable to an empty settler. The following passage shows the comparison between the laboratory-scale settler experiments and the modified modelling approach, as well as a modelling test for scale-up of the settler. Table 5 shows a comparison between the experiments and the modelling of a DN 100 settler using the following boundary conditions:

$$\dot{V}_{\text{in}} = 0.2 \frac{\text{m}^3}{\text{h}}, \alpha_0 = 0.2; 0.3, L_{\text{ac}} = 0.18 \, \text{m}, L_{\text{mesh}} = 0.05, h_{\text{ac}}$$
$$= 0.01 - 0.023 \, \text{m}, r_{\text{S}}^* = 0.033, D_{\text{s}} = 0.1 \, \text{m}, D_{\text{in}}$$
$$= 0.015 \, \text{m}, L_{\text{s}} = 1 \, \text{m}, D_{32,0} = 500 \, \mu\text{m}, t_{\text{coal}} = 0.76$$

Figure 17 shows the length of the dispersion wedge in the experiment with the phase fraction variation over time using a 50 mm stainless-steel knitted mesh. The images show that at a phase fraction of 30%, the knitted mesh is not able to fully reduce the dispersion anymore and, behind the mesh, a dispersion wedge forms. The adapted model is able to reproduce the measured wedge lengths in the experiments after the knitted mesh. This allows for a calculation of the reduction of the wedge length compared to the settler without a mesh and is used in the following cases to investigate the scale-up of a settler using different assumptions.

The first case assumes that the accumulation height of the dispersion in front of the mesh is not affected by the change in diameter of the settler from DN100 to DN200 (0.1–0.2 m). Only the flow rate is adapted to the larger diameter of the settler. For this, it is assumed that the superficial liquid velocity in the settler is the same as in the smaller settler. This results in a higher flow rate of $\dot{V}_{\text{in}} = 0.8 \frac{\text{m}^3}{\text{h}}$. All the other boundary conditions remain constant. Table 6 shows the results of the modelling approach for a DN200 settler.

The model shows that the higher throughput in the larger settler leads to an earlier breaching point of the dispersion wedge when using the same 50 mm stainless-steel knitted mesh as in the smaller settler. The second case assumes that the accumulation of the dispersion in front of the mesh is linearly dependent on the wedge length. This factor is calculated in Table 7 and then used to calculate the accumulation height from the predicted wedge length in the larger settler using the standard model (see Table 8).

Table 9 shows the modelling results in this case. Because of the higher accumulation in front of the mesh, the wedge length behind the mesh is reduced compared to the previous results. The longer mesh reduces the wedge at a higher rate than the 50 mm mesh. This can be explained through the assumption of a linear decreasing

TABLE 8 Calculation of the scale-up factor with constant accumulation rate of the dispersion in front of the mesh, based on dispersion wedge length

Phase fraction	Henschke (DN200) (mm)	Factor	Factor
20%	470	0.039	470 mm · 0.0039 = 18.33 mm
30%	660	0.059	660 mm · 0.059 = 38.94 mm

TABLE 9 Scale-up modelling with a constant accumulation rate of the dispersion in front of the mesh, based on dispersion wedge length

Phase fraction	Henschke (cm)	Henschke modified VA50 (after mesh) (cm)	Henschke modified VA200 (after mesh) (cm)
20%	47	39 (16)	30 (0)
30%	66	58 (35)	44 (6)

TABLE 10 Scale-up with halved accumulation height of the dispersion in front of the mesh

Phase fraction	Henschke (cm)	Henschke modified VA50 (after mesh) (cm)	Henschke modified VA200 (cm)
20%	47	43 (20)	35 (0)
30%	66	66 (25)	54 (16)

dispersion height in the mesh and is in accordance with the observations in the experiments.

The third case assumes that the accumulation of the dispersion is smaller in the larger settler. The reasoning behind this is that for a settler without internals, the dispersion wedge in a larger settler is usually shallower and longer compared to smaller vessels.[19] The dispersion has a higher area to spread out, compared to the smaller settler. For this modelling, the accumulation height of the experiments is halved in the larger settler. This results in an overall longer dispersion wedge and a smaller reduction of the dispersion via the knitted mesh. The modelling experiments can give an insight over the best- and worst-case scenarios during scale-up of the settler and allow an estimate of the maximal needed settler length (see Table 10).

5 | CONCLUSIONS

Gravity settlers play an important role in many chemical engineering applications. The settling characteristics of a dispersion is strongly dominated by the DSD involved. Its measurement using optical imaging approaches has many challenges. One of them is the segmentation of the particles at higher phase fractions. This work develops a state-of-the-art machine learning approach using a CNN and a solution to the database generation using a fully algorithmic approach, based on a previous work.[14] From there, a representative system of computationally generated spherical droplets can be used for training in a first step. Based on this trained CNN, a second network can be trained to directly segment the droplet images. This allowed the final segmentation of the particulate system without the need to own already evaluated images, which were being used in the training process.

For an investigation of knitted meshes as coalescing aids, the CNN segmentation approach was implemented into the automated control loop of the mixer-settler. The automated image analyses allowed to control a set, for example, mean diameter when variating specific conditions (phase ratio, throughput). The experiments exemplified a different behaviour depending on the wetting characteristics of the fibre materials used. In a basic study in a DN100 mixer-settler, different meshes (porosity, fibre thickness, and length) of different structures (wrapped and layered) and materials (perfluoroalkoxy alkane, stainless steel, and mixed with glass) in the system of water/paraffin were investigated.

The experiments revealed a linear accumulation of the dispersion height within the mesh. The results of the experiments were used to develop an extension of an established iterative design approach for the implementation of knitted meshes as coalescing aids in horizontal gravity settlers.

NOMENCLATURE
Symbols
A	area (m^2)
D	diameter (m)
d_{10}	mean diameter from first and zero moment (m)
d_{32}	mean Sauter diameter (m)
$\vec{g}$	gravitational constant (ms^{-2})
H	initial height (m)
H_{cd}	Hamaker coefficient (−)
h	height (m)
L	length (m)
Lr	learning rate (−)
M	mass (kg)
m_m	momentum (−)

n	number $(-)$
Δp	pressure difference (Pa)
$\overline{p}$	mean pressure (Pa)
$R_a,$	droplet radius in the asymmetric coalescence
R_f	model (m)
r_s^*	dimensionless coalescence parameter $(-)$
t	time (s)
V	volume (m^3)
$\dot{V}$	volumetric flow rate (m^3/h)
w	weight decay $(-)$

Greek letters

A	phase fraction
μ	dynamic viscosity (kg m^{-1} s^{-1})
ρ_{pa}	packing density (kg/m^3)
σ	interfacial tension (kg s^{-2})
τ_{di}	coalescence time

Subscripts

ac	accumulation of the dispersion
ci	circle
co	contour
coal	coalescence
dis	dispersion
free	free
i	index
in	in
l	length
mesh	mesh
p	packed dispersion
s	settler
0	start

Dimensionless numbers

Ar	Archimedes number
La$_{mod}$	modified Laplace number
Re	Reynolds number

Abbreviations

CNN	convolutional neuronal network
COMB	combination
DN	diameter nominal
DSD	drop size distribution
LED	light emitting diode
OMOP	optical multimode online probe
PFA	perfluoro alkyloxy alkane
RPM	rotation per minute
VA	stainless steel

AUTHOR CONTRIBUTIONS

Jan Schäfer: Data curation; investigation; software; writing – original draft; writing – review and editing. **Mark W. Hlawitschka:** Software; supervision; validation; writing – review and editing. **Hans-Jörg Bart:** Conceptualization; project administration; resources; supervision; writing – review and editing.

ACKNOWLEDGEMENTS

PEER REVIEW

The peer review history for this article is available at https://publons.com/publon/10.1002/cjce.24503.

DATA AVAILABILITY STATEMENT

The data that support the findings of this study are openly available in [urn:nbn:de:hbz:386-kluedo-65339] at https://doi.org/10.26204/KLUEDO/6533.

ORCID

Jan Schäfer https://orcid.org/0000-0002-2328-8153
Mark W. Hlawitschka https://orcid.org/0000-0003-2580-1886
Hans-Jörg Bart https://orcid.org/0000-0002-2555-8989

REFERENCES

[1] H.-J. Bart, G. Stevens, in *Ion Exchange and Solvent Extraction*, Vol. 17 (Eds: M. Kertes, A. K. Sengupta), Marcel Dekker, New York **2004**, p. 37.

[2] H. Franken, personal communication (**2016**).

[3] M. Kraume, *Mischen und Rühren*, Wiley, Weinheim, Germany **2002**.

[4] J. Steinhoff, *Ph.D. Thesis*, TU Kaiserslautern (Kaiserslautern, Germany) **2020**.

[5] J. Steinhoff, E. Charlafti, L. Reinecke, M. Kraume, H.-J. Bart, *Can. J. Chem. Eng.* **2020**, *98*, 384.

[6] T. Pilhofer, H.-D. Miller, *Chem. Ing. Tech.* **1972**, *44*, 295.

[7] G. Besagni, P. Brazzale, A. Fiocca, F. Inzoli, *Flow Meas. Instrum.* **2016**, *52*, 190.

[8] H.-M. Prasser, D. Scholz, C. Zippe, *Flow Meas. Instrum.* **2001**, *12*, 299.

[9] S. Maaß, S. Wollny, A. Voigt, M. Kraume, *Exp. Fluids* **2011**, *50*, 259.

[10] S. Rabha, M. Schubert, M. Wagner, D. Lucas, U. Hampel, *AIChE J.* **2013**, *59*, 1709.

[11] M. Schlüter, *Chem. Ing. Tech.* **2011**, *83*, 992.

[12] M. Lichti, H.-J. Bart, *Flow Meas. Instrum.* **2018**, *60*, 164.

[13] H.-J. Bart, M. Mickler, H. Jildeh, in *Optical Imaging: Technology, Methods & Applications*, Vol. 1 (Eds: A. Tanaka, B. Nakamura), Nova Science, Lancaster, UK **2012**.

[14] J. Schäfer, P. Schmitt, M. W. Hlawitschka, H.-J. Bart, *Chem. Ing. Tech.* **2019**, *91*, 1688.

[15] W. Rawat, Z. Wang, *Neural Computation* **2017**, *29*, 2352.

[16] Y. LeCun, Y. Bengio, G. Hinton, *Nature* **2015**, *521*, 436.

[17] O. Ronneberger, P. Fischer, T. Brox, in *Medical Image Computing and Computer-Assisted Intervention – MICCAI*. Lecture Notes in Computer Science, Vol. 9351 (Eds: N. Navab, J. Hornegger, W. M. Wells, A. F. Frangi), Springer International Publishing, Cham, Switzerland **2015**, p. 34.

[18] J. Schäfer, *Ph.D. Thesis*, TU Kaiserslautern (Kaiserslautern, Germany) **2021**.

[19] M. Henschke, *Ph.D. Thesis*, RWTH Aachen (Aachen, Germany) **1995**.

[20] S. Hu, R. C. Kinter, *AIChE J.* **1955**, *1*, 42.

[21] A. J. Klee, R. E. Treybal, *AIChE J.* **1956**, *2*, 444.

[22] M. Ishii, N. Zuber, *AIChE J.* **1979**, *25*, 843.

[23] C. A. Coulaloglou, L. L. Tavlarides, *Chem. Eng. Sci.* **1977**, *32*, 1289.

[24] M. J. Prince, H. W. Blanch, *AIChE J.* **1990**, *36*, 1485.

[25] L. Schlieper, M. Chatterjee, M. Henschke, A. Pfennig, *AIChE J.* **2004**, *50*, 802.

AUTHOR BIOGRAPHIES

Jan Schäfer studied business economics with a specialization in environmental and process engineering at TU Kaiserslautern. In 2021, he completed his doctorate at TU Kaiserslautern on the investigation of knitted meshes in horizontal gravity settlers and the modelling of the bubble size distribution in CFD investigations of bubble columns. Since 2020, he has been a researcher at Helmholtz Zentrum Dresden Rossendorf.

Mark W. Hlawitschka studied mechanical and process engineering at the TU Kaiserslautern. In 2013, he completed his doctorate at the TU Kaiserslautern on the topic of solvent extraction. In 2013, he was a project leader/post doc. In 2019, Mark Hlawitschka habilitated on the topic of reactive bubble columns. Since October 2020, he has been the head of the Institute of Process Engineering at JKU Linz. His research topics include the investigation of the interaction between hydrodynamics and (reactive) mass transfer, (reactive) solvent extraction, and the investigation of detailed phenomena such as coalescence or fouling.

Hans-Jörg Bart studied chemical engineering at TU Graz, Austria, and finished his PhD in 1982. He was finally there as an associate professor and head of the Christian Doppler Laboratory (Modelling of Reactive Systems). From 1994 to 2020, he was a tenured professor (Thermische Verfahrenstechnik) at TU Kaiserslautern, Germany. He is now a senior research professor and chairman of the International Committee for Solvent Extraction, and his research interests are in polymeric heat exchangers, fluid dynamics, population balances, and image analysis of particles (bubbles, droplets, crystals, etc.) via optical sensors.